

# EUV Mask Multilayer Defects and Their Printability under Different Multilayer Deposition Conditions

Hyuk Joo Kwon\*, Jenah Harris-Jones, and Aaron Cordes  
SEMATECH, 257 Fuller Rd. Suite 2200, Albany, NY 12203 USA

Masaki Satake and Ying Li  
Luminescent Technologies, 2471 East Bayshore Rd. Suite 600, Palo Alto, CA, 94303 USA

Iacopo Mochi and Kenneth A. Goldberg  
Center for X-ray Optics, LBNL, 1 Cyclotron Road Berkeley, CA 94720 USA

## ABSTRACT

Extreme ultraviolet (EUV) patterning appears feasible using currently available EUV exposure tools, but some issues must still be resolved for EUV patterning to be used in production. Defects in EUV mask blanks are one such major issue and inspection tools are needed to detect phase defects on EUV mask blanks that could possibly print on the wafer. Currently available inspection tools can capture defects on the mask, but they also need to be able to classify possible printable defects. Defect classification for repair and mitigation of printable defects is very difficult using deep ultraviolet (DUV) inspection tools; however, if the actinic inspection tool (AIT) could gather defect information from more multilayer (ML) stacks, it may be able to separate printable defects from unprintable defects. If unprintable defects could be eliminated, the defect information could be used for mask pattern shifts to reduce printable defects. Fewer defects would need to be repaired if there were a better chance of capturing printable defects using an actinic inspection tool. Being able to detect printable defects on EUV blanks is therefore critical in mask making.

In this paper, we describe the characterization of programmed ML phase defects in the manufacturing of EUV mask blanks using the state-of-the-art mask metrology equipment in SEMATECH's Mask Blank Development Center (MBDC). Programmed defects of various dimensions were prepared using e-beam patterning technology and Mo/Si MLs were deposited with SEMATECH's best known method (BKM) and pit smoothing conditions on programmed defects to characterize ML phase defects. Atomic force microscopy (AFM) and transmission electron microscopy (TEM) were used to study ML profile changes, while SEMATECH's AIT was used to image ML phase defects and predict their printability. Multilayer defect reconstruction (MDR) was done using AFM images, which were then compared to TEM images. Defect printability simulation (DPS) was used for comparison to AIT through-focus images. 22 nm, 27 nm, and 32 nm line and space (L/S) absorber patterns were positioned on top of programmed ML phase defects and simulated defect printability. The ML phase defects are located at the edge of L/S patterns and at the center of space patterns and Bossung plot was used to separate printable defects from unprintable defects.

**Keywords:** Defect printability, programmed multilayer defect, multilayer phase defect, multilayer defect reconstruction, defect printability simulation.

## 1. INTRODUCTION

While EUV wafer patterning appears feasible with currently available exposure tools (NXE3100), some issues must still be solved for EUV patterning to be used in production. The major challenges are the source power/lifetime and mask defect/contamination control. Because defects in EUV mask blanks are one such major issue, much research is focusing on defect printability.<sup>1-7</sup> Absorber defects, which can be detected as clear and opaque defects and particles, are common to conventional optical masks. However, EUV masks have ML phase defects that must be classified. Although their dimensions can be characterized using currently available metrology tools, native phase defects

---

\* [harry.kwon@sematech.org](mailto:harry.kwon@sematech.org) or [hyukjoo.kwon@samsung.com](mailto:hyukjoo.kwon@samsung.com); Phone: (518) 649-1160; Fax: (518) 649-1344

cannot be realistically characterized without knowledge of defect-induced changes in the structure of the deposited ML. Mask defects from MLs can be classified as shown in figure 1. Inspection tools detect defects, but they also need to separate the false and real defects, which depends on inspection tool parameters. With real defects, the printable must be separated from the unprintable. To detect printable defects, a defect printability study using blank inspection (BI), patterned mask inspection (PMI), and an aerial image metrology system (AIMS) is needed. If a ML defect with L/S absorber patterns is exposed at the exposure tool, the critical dimension (CD) of the wafer can be used to decide which blank defects will print and which will not. The process window for blank defects on wafers will usually be decided by Bossung plots and DPS will be used to separate printable from unprintable defects using the Bossung plot.

In this paper, we prepare programmed and characterized ML defects. Programmed defects of various dimensions were prepared using e-beam patterning technology. Because ML phase defect printability is strongly dependent on the ML deposition condition, Mo/Si MLs were deposited under SEMATECH's BKM and pit smoothing conditions on programmed defects to characterize ML phase defects after different deposition conditions. AFM and TEM were used to study ML profile changes, while SEMATECH's AIT was used to image ML phase defects and predict their printability using ThroughFocus analysis software. MDR was done using AFM images, which compared to TEM images. DPS was used for comparison to AIT through-focus images. 22 nm, 27 nm, and 32 nm L/S absorber patterns were positioned on top of programmed ML phase defects and simulated phase defect printability. The ML defects are located at the edge and at the center of L/S patterns. Bossung plots were used to separate printable defects from unprintable defects. Defect printability under different illumination conditions was evaluated.

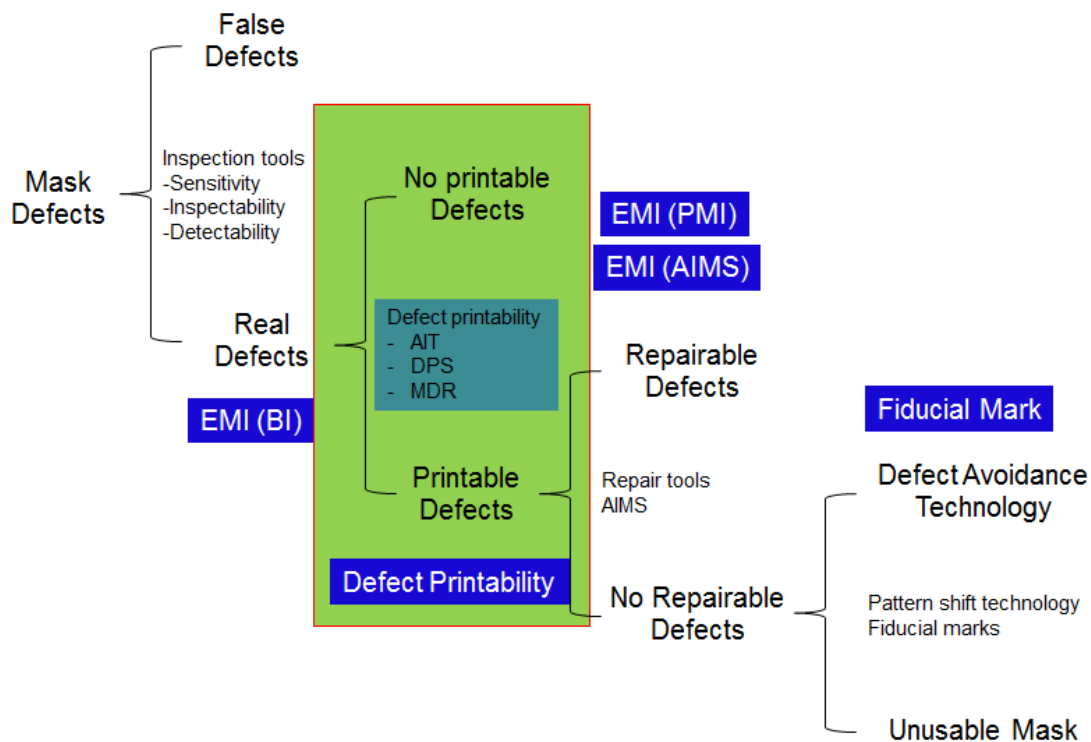


Figure 1. Classifications of EUV mask defects. EMI: EUV Mask Infrastructure.

## 2. EXPERIMENTAL PROCEDURE

Figure 2 shows the procedure to manufacture programmed ML phase defects. Ru and TaON layers were deposited on quartz plates. The Ru layer is used as the etch stop layer during programmed defect formation. The TaON layers were patterned by conventional e-beam writing, followed by resist coating, e-beam exposure, resist develop, dry etch, resist strip, and cleaning. MLs were deposited on top of the programmed defects under SEMATECH's BKM

and pit smoothing conditions using an ion beam deposition (IBD) tool in SEMATECH's MBDC. Two ML deposition conditions are obtained by changing the substrate angle (SA) and the target angle (TA) of the IBD tool. Defect dimensions were measured before and after ML deposition using AFM. The programmed defects were inspected at the SEMATECH's AIT and analyzed using ThroughFocus software. TEM images to get cross-sectional images of programmed ML phase defects were obtained and DPS was done using MDR images as input data for DPS to see Bossung plots of the phase defects.

Figure 3 shows the procedure of DPS. Dimensions from AFM and TEM were used to generate the ML structure, and MDR parameters for ML defects were obtained. MDR images were obtained using only AFM images by employing MDR parameters. The MDR images were used for input parameters for DPS. Image intensities from DPS were compared to AIT image intensities and wafer images from both DPS and AIT results were compared at the through-focus region from -50 nm to +50 nm. DPS was also used to study printability at L/S patterns as shown in figure 4. Programmed ML phase defects are located at the edge of L/S patterns and at the center of space patterns for 22 nm, 27 nm, and 32 nm L/S printability simulations. Dimensions of programmed ML phase defects for the simulations are full width at half maximum (FWHM) of 20 nm to 80 nm with depths of 1 nm to 4 nm at the bottom of the MLs. Image intensities were obtained using MDR images with L/S patterns and defect printability images were analyzed using DPS to determine whether or not the defects will print on the wafers.

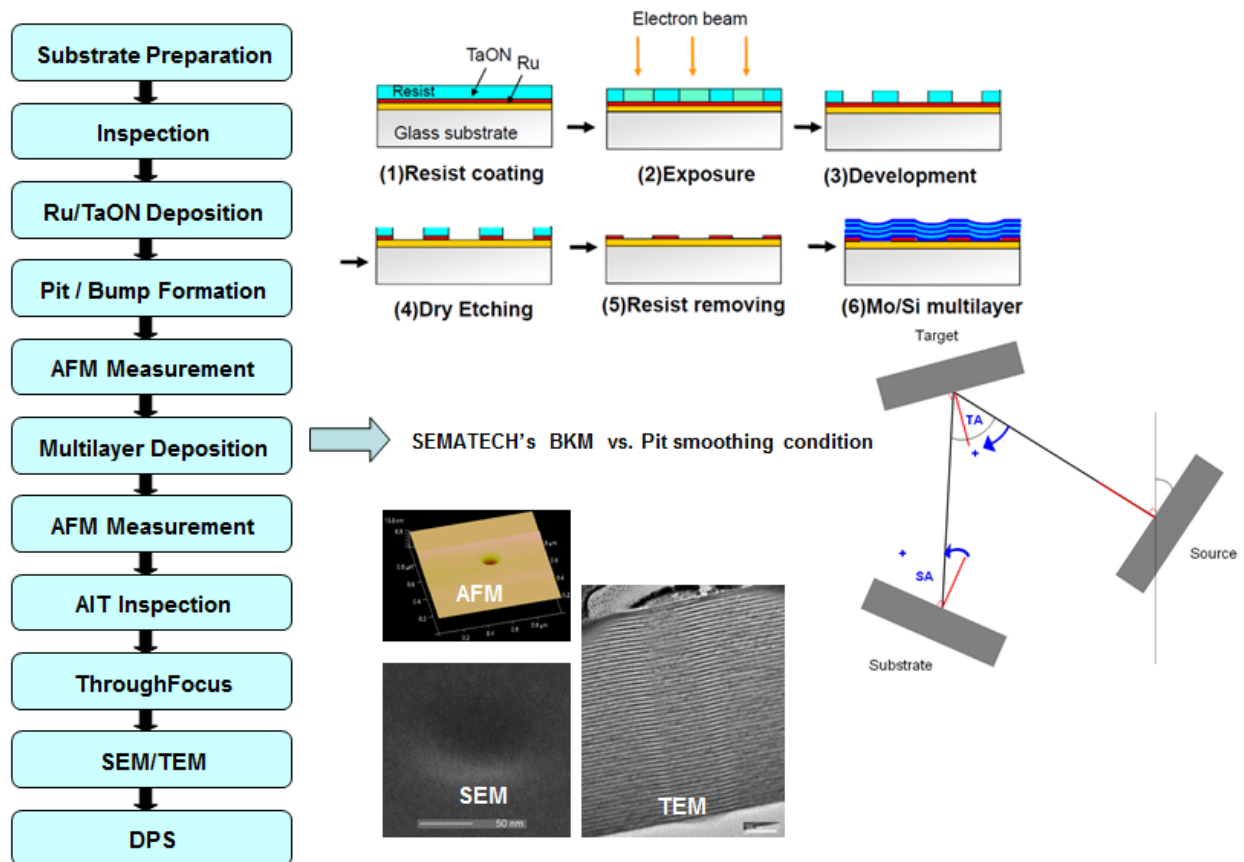


Figure 2. Experimental procedure for programmed ML phase defects.

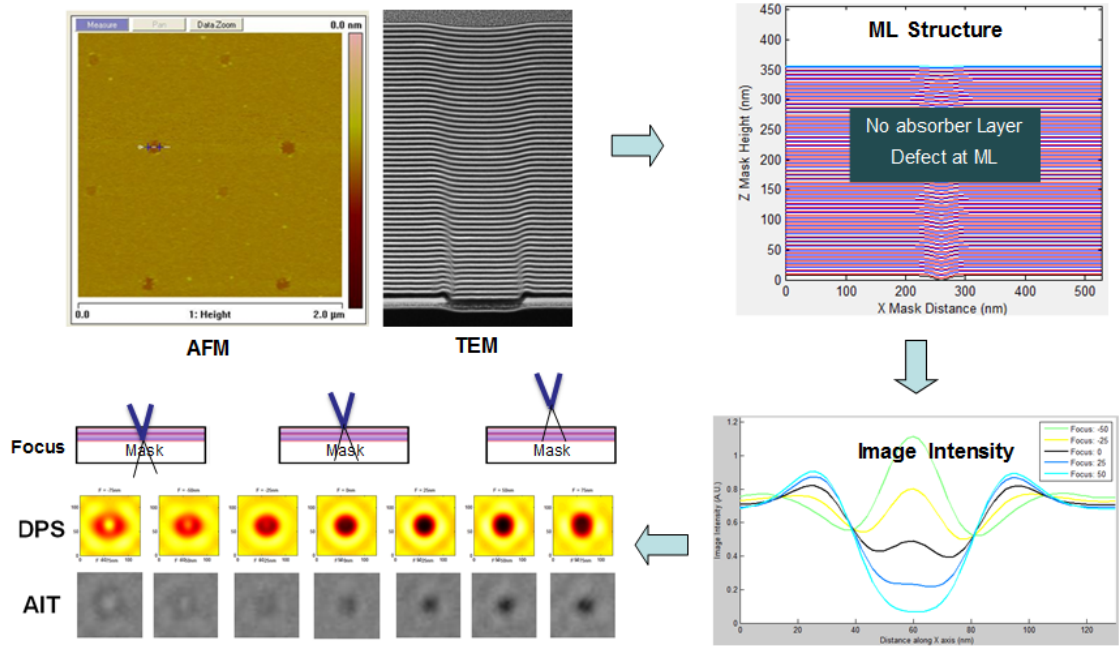


Figure 3. Procedure to simulate defect printability.

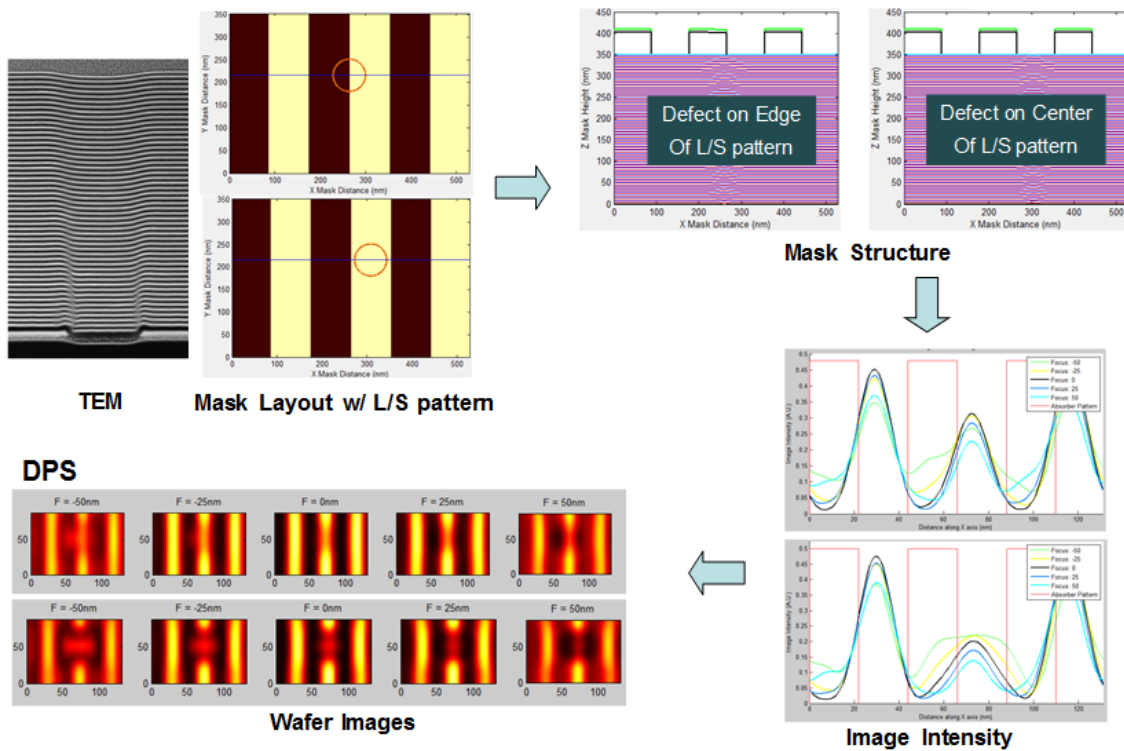


Figure 4. Defect printability simulation for L/S patterns. 22nm, 27 nm, and 32 nm L/S patterns were simulated.

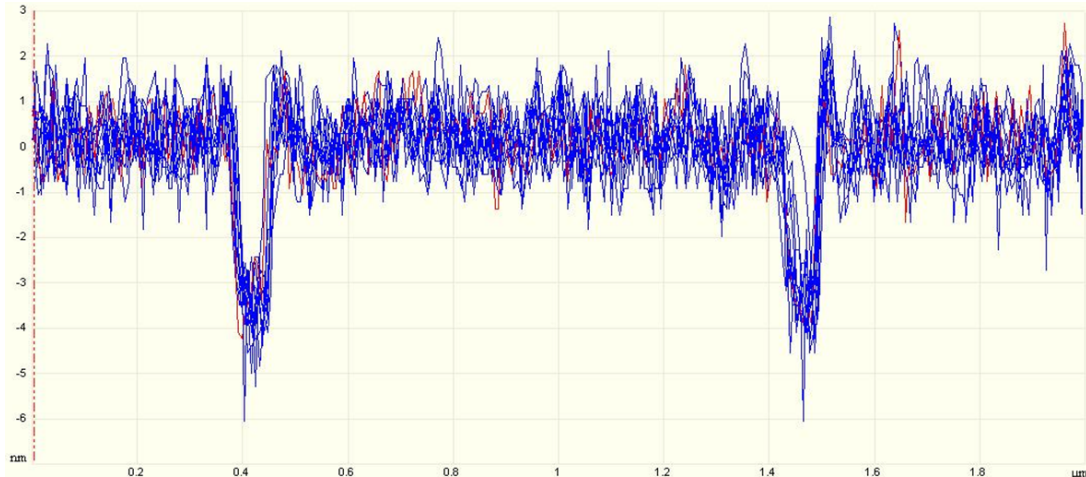


Figure 5. Signal from AFM measurement.

Stack structure for programmed ML phase defect simulation is 50 bi-layers for ML layers with 51 nm TaN and 7 nm TaON for absorber layers. The illumination condition for DPS was set to 0.2 sigma and 0.35 NA, which are identical to AIT illumination conditions. The incident angle of the EUV light source was 6 degrees for both AIT and DPS. However, magnification of mask images to wafer images for AIT was 980 and for DPS was 0.25. Ranges of dose and focus for the Bossung plots were set to 95 % to 105 % and -50 nm to + 50 nm, respectively. The focus step was set to 25 nm. To classify the phase defects for printable and unprintable defects, process margins of 22 nm +/- 2nm, 27 nm +/- 2.5 nm, and 32 nm +/- 3 nm were set to separate printable and unprintable regions. If L/S patterns generated by the exposure tool on the wafer from ML phase defects were within the process margin, the defects were classified as unprintable defects, which do not need to be repaired. Dimensions for ML defects were obtained from AFM and TEM. However, the depths of the programmed defects were almost less than 4 nm and signals from the AFM measurement have significant noise as shown in figure 5. Therefore, the AFM signal was flattened and filtered to use the depths for MDR and DPS for depth analysis. The depths (rms) from AFM were used for general printability trend analysis and multilayer decoration analysis because we could not get TEM images for all phase defects. Depths from TEM were used for defect printability simulations for specific phase defect analysis. The depths from AFM and TEM show the relationship as follows:

$$\text{AFM Depth (rms)} < \text{Depth (TEM)} < \text{AFM Depth (max)}$$

### 3. RESULTS AND DISCUSSION

#### 3.1 Decoration of programmed ML phase defects

Figure 6 shows the characteristics of programmed ML phase defects. The ML was deposited under SEMATECH's BKM condition. The FWHM of programmed ML phase defects increases during the ML depositions, but the depths of programmed ML phase defects decreases during ML depositions. Defect dimensions of programmed ML defects were given as follows.

$$(\text{Depth of defect after ML deposition}) = 0.63 \times (\text{Depth of defect before ML deposition})$$

$$(\text{FWHM of defect after ML deposition}) = (\text{FWHM of defect before ML deposition}) + 21$$

However, the AFM signal has a lot of noise because the defect dimensions are on the order of nanometers, as shown in figure 5. On the other hand, when the ML was deposited using the pit smoothing condition, the dimensions of the programmed ML phase defects cannot be measured at the top of ML by AFM. Because the AFM detection limit is

less than 0.5 nm, the dimensions of the ML phase defects at the top are less than 0.5 nm. When the defects with a FWHM of 58.5 nm and depth of 1.7 nm at the bottom of the ML were inspected with the AIT, the AIT image was captured as shown in figure 7.

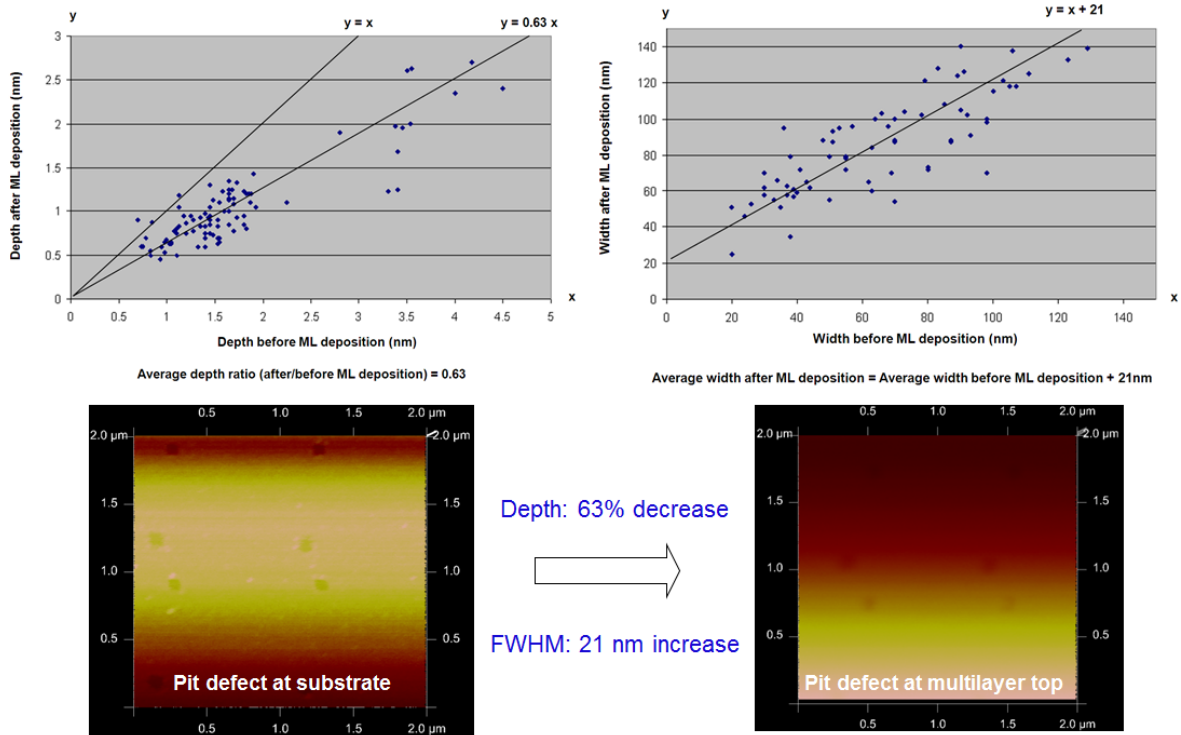


Figure 6. Defect decoration of programmed defects. The ML was deposited under SEMATECH's BKM condition.

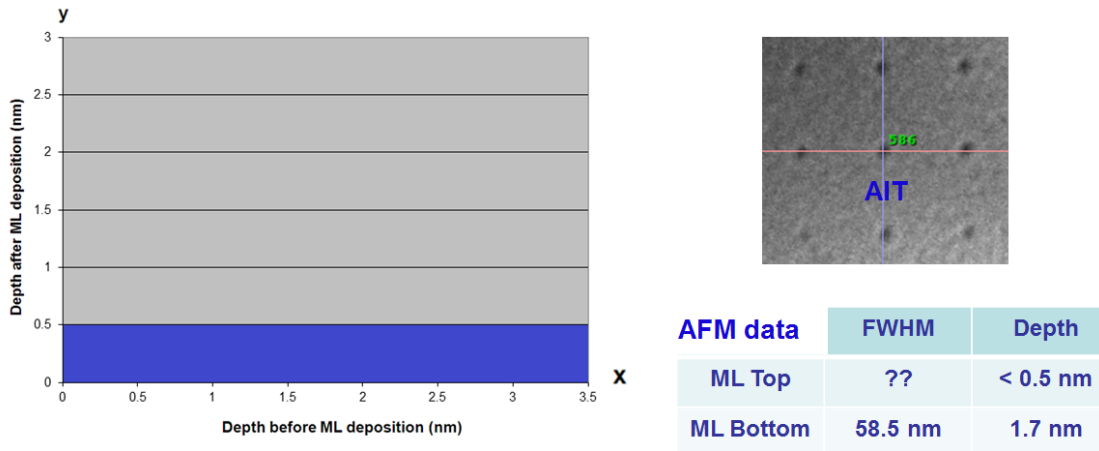


Figure 7. Defect decoration of programmed defects. The ML was deposited under the pit smoothing condition.

### 3.2 MDR

Dimensions of ML phase defects were measured by AFM and TEM to extract MDR parameters. The MDR parameters were optimized for generic MDR for arbitrary defects. Using the optimized MDR parameters, ML defects of arbitrary shapes were reconstructed using only AFM images of the ML top surface. Figure 8 shows an example of the MDR images. The blue lines are predicted ML profiles obtained from MDR simulation software and the predicted ML profiles are overlaid on the actual TEM images. The MDR images using only top surface AFM data match actual TEM images well. The ML structure regenerated from MDR was used for inputs to DPS as shown in figures 3 and 4.

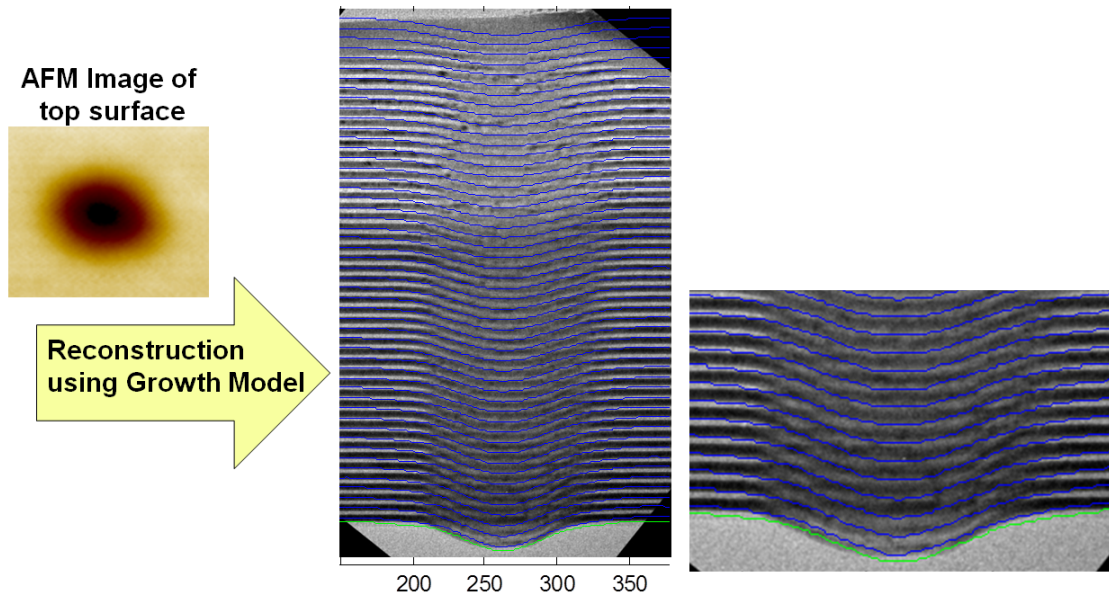


Figure 8. ML reconstruction images. Blue lines are predicted ML profiles overlaid on actual TEM images.

### 3.3 AIT vs. DPS

Through-focus images of ML phase defects were obtained with the AIT using 0.2 sigma and 0.35NA. DPS aerial intensities were calculated at the same illumination condition as the AIT and then were compared with AIT intensities as shown in figure 9. AIT intensities and DPS aerial intensities were obtained from ML phase defects without absorber layers. The DPS aerial intensity profiles were well matched with the AIT intensity profiles.

### 3.4 DPS for native ML phase defects

Dimensions for native ML phase defects were obtained from SEMATECH's defect library which is reported elsewhere.<sup>7,8</sup> Figure 10 shows the dimensions of native ML phase defects and the characteristics of defect decoration. Most native ML phase defects captured by inspection tools are large enough to be classified as printable defects. Therefore, dimensions for programmed ML phase defects designed to be smaller than native ML phase defects. Programmed ML phase defects have a FWHM of less than 80nm with depths of less than 4 nm for the DPS study as shown in figure 10. One native ML phase defect was selected for the DPS. The dimensions of the native ML phase defect are FWHM of 28 nm with a 5.2 nm depth at the bottom of the ML and FWHM of 62 nm with a 4 nm depth at the top of the ML. The printability for 22 nm, 27 nm, and 32 nm L/S were obtained when the native ML phase defects were located at the edge of L/S patterns and at the center of space patterns as shown in figure 11. The native defect is printable at the focus range of -50 nm to 50 nm at 22 nm, 27 nm, and 32 nm L/S patterns. The defect is less printable when it is located at the edge of L/S pattern than when at the center of the space pattern. Therefore, ML phase defects with smaller dimension than this native defect must be analyzed.

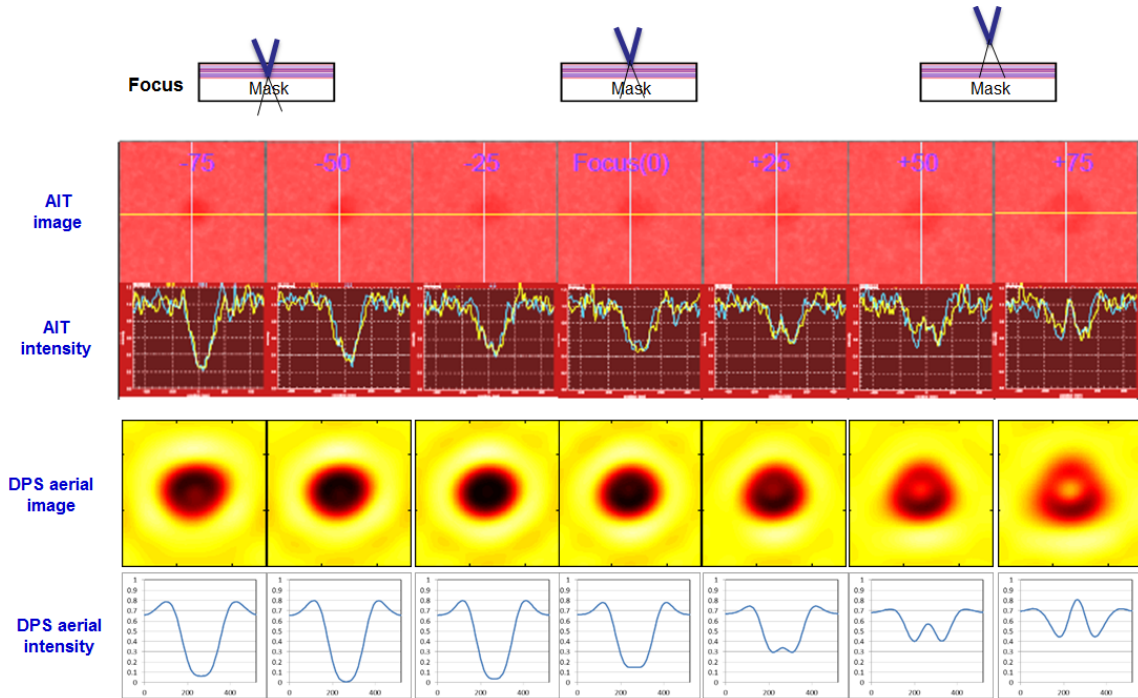


Figure 9. Comparison of AIT and DPS intensity.

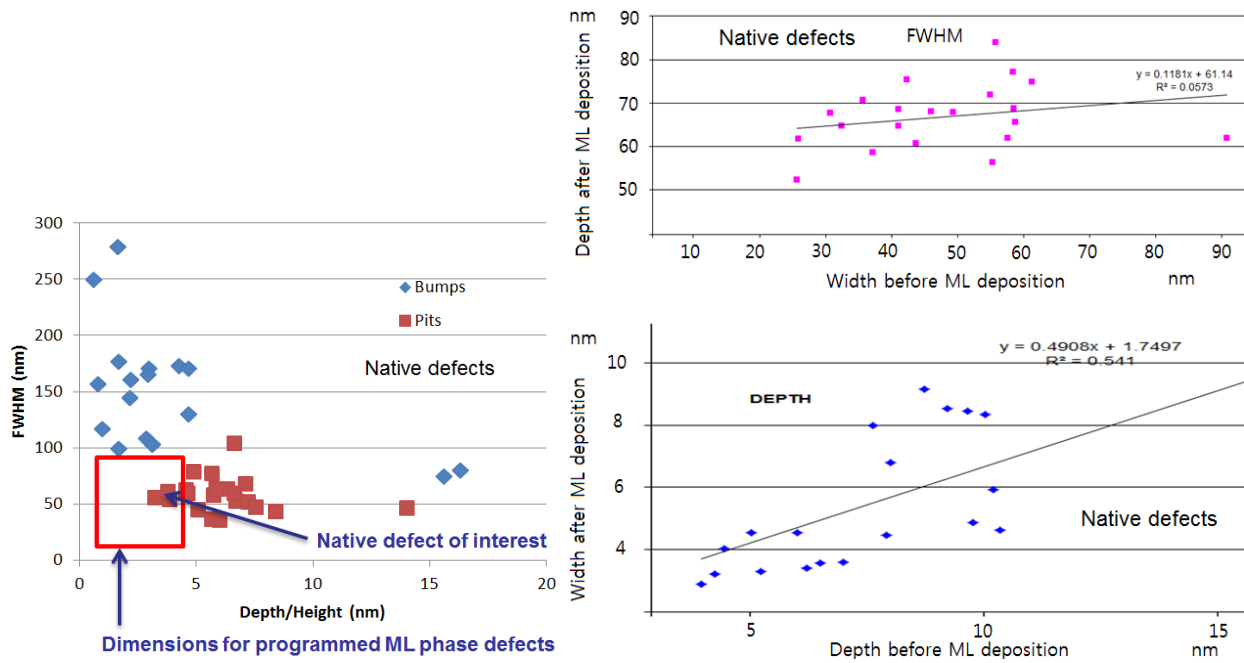


Figure 10. Dimensions for native and programmed ML phase defects. Most native ML phase defects have larger dimensions than programmed ML phase defects. Red box represents dimensions of programmed ML phase defects designed for the regions of interest for DPS.



Figure 11. DPS images for a native ML phase defect.

### 3.5 DPS for programmed ML phase defects

Figure 12 and figure 13 show DPS images of programmed ML phase defects with different defect dimensions. The ML was deposited under SEMATECH's BKM condition. The programmed ML phase defect in figure 12 is smaller size than that in figure 13. Therefore, the defect in figure 12 is less printable than in figure 13. When defects are located at the edge of L/S patterns, the defects are less printable than when they are located at the center of space patterns.

Figure 14 and figure 15 show DPS images for programmed ML phase defects of different dimensions that were deposited under pit smoothing conditions. Phase defects were not detected by AFM at the top of the ML and the dimensions of the phase defects at the top were less than 0.5 nm, which are within the AFM detection limit. However, intensity images were obtained by AIT. Likewise, defects at the edge of L/S patterns are less printable than those at the center of clear patterns; the smaller defect in figure 14 is less printable than the larger defect in figure 15. When ML deposition conditions are compared, the defects deposited under pit smoothing condition are less printable than those at SEMATECH's BKM condition. The defects at pit smoothing conditions have an almost flat surface on top of the ML and the defect at the top acts like a defect without phase. However, TEM images need to be obtained for more thoroughly analyze defect decoration during ML deposition. Because the printability of programmed ML phase defects is strongly dependent on ML deposition conditions, they must be optimized to yield fewer printable defects on the wafers, even though the same defects are at the bottom of the ML.

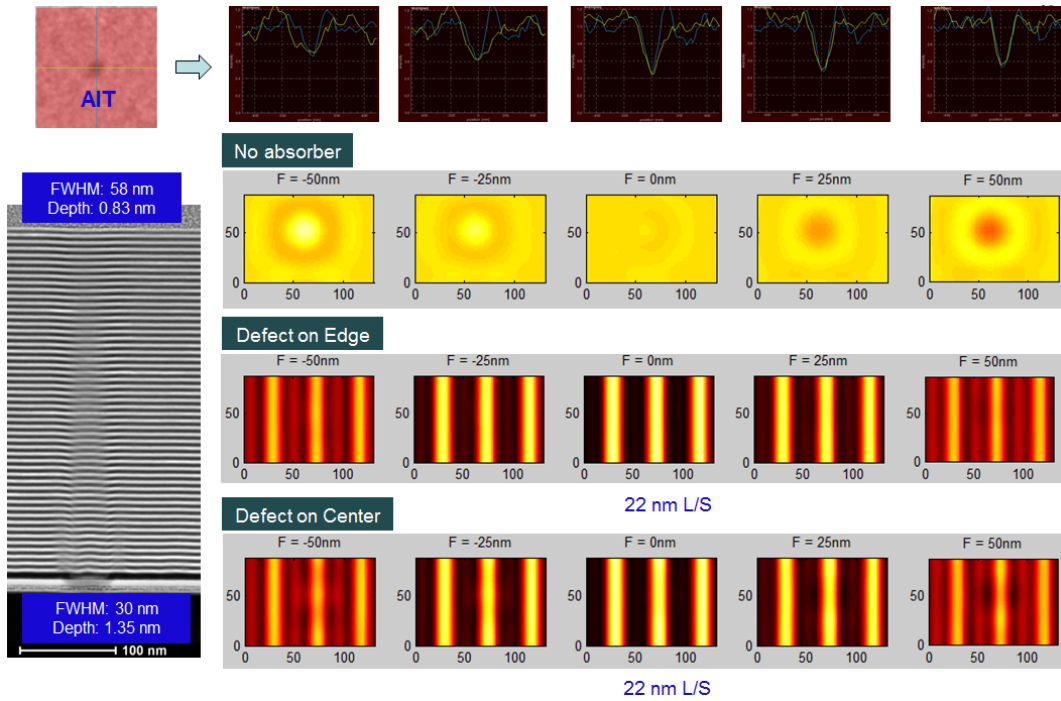


Figure 12. DPS images for a programmed ML phase defect. ML was deposited under SEMATECH's BKM condition. Dimensions: FWHM of 30 nm with 1.35 nm depth at the bottom of the ML and FWHM of 58 nm with 0.83 nm depth at the top of the ML.

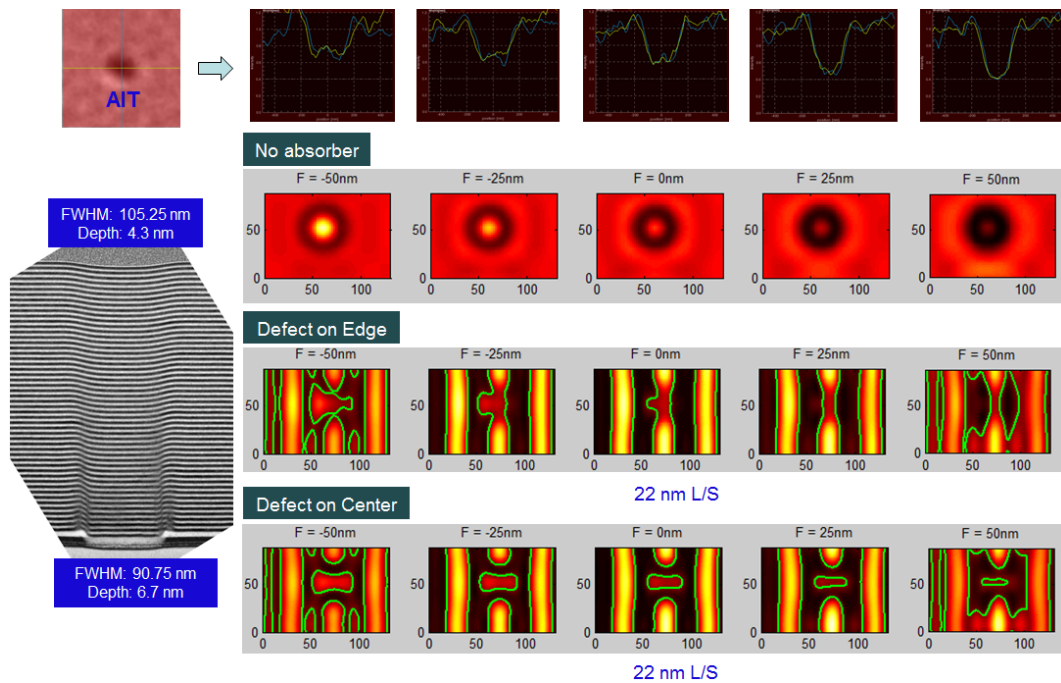


Figure 13. DPS images for a programmed ML phase defect. ML was deposited under SEMATECH's BKM condition. Dimensions: FWHM of 90.75 nm with 6.7 nm depth at the bottom of the ML and FWHM of 105.25 nm with 4.3 nm depth at the top of the ML.

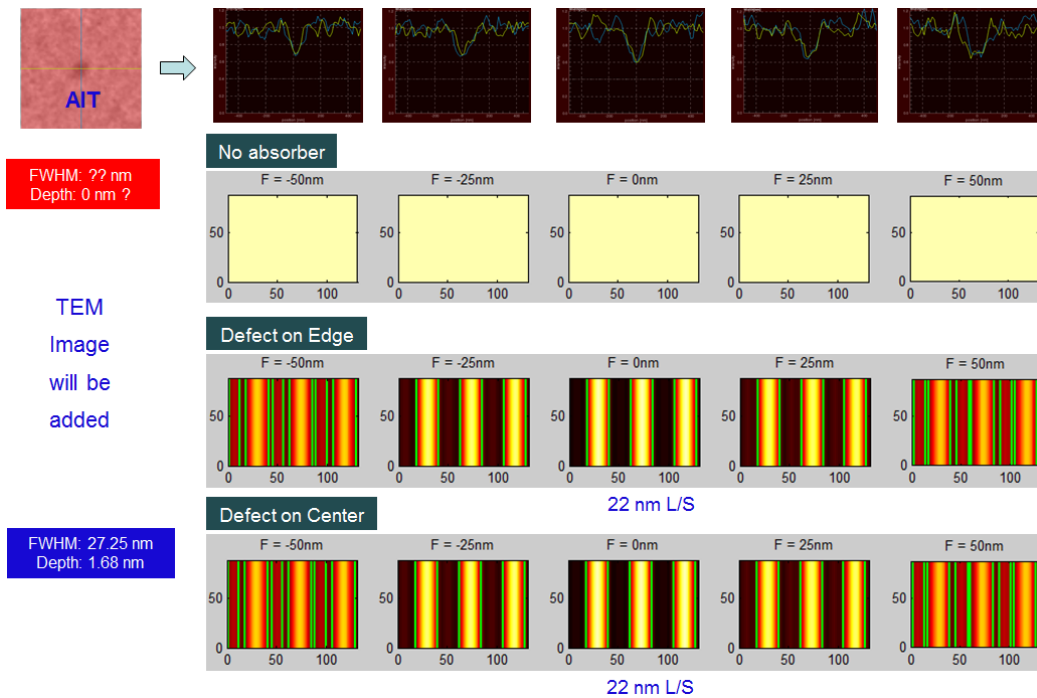


Figure 14. DPS images for a programmed ML phase defect. ML was deposited under pit smoothing conditions. Dimensions: FWHM of 27.25 nm with 1.68 nm depth at the bottom of the ML. No AFM image at the top of the ML.

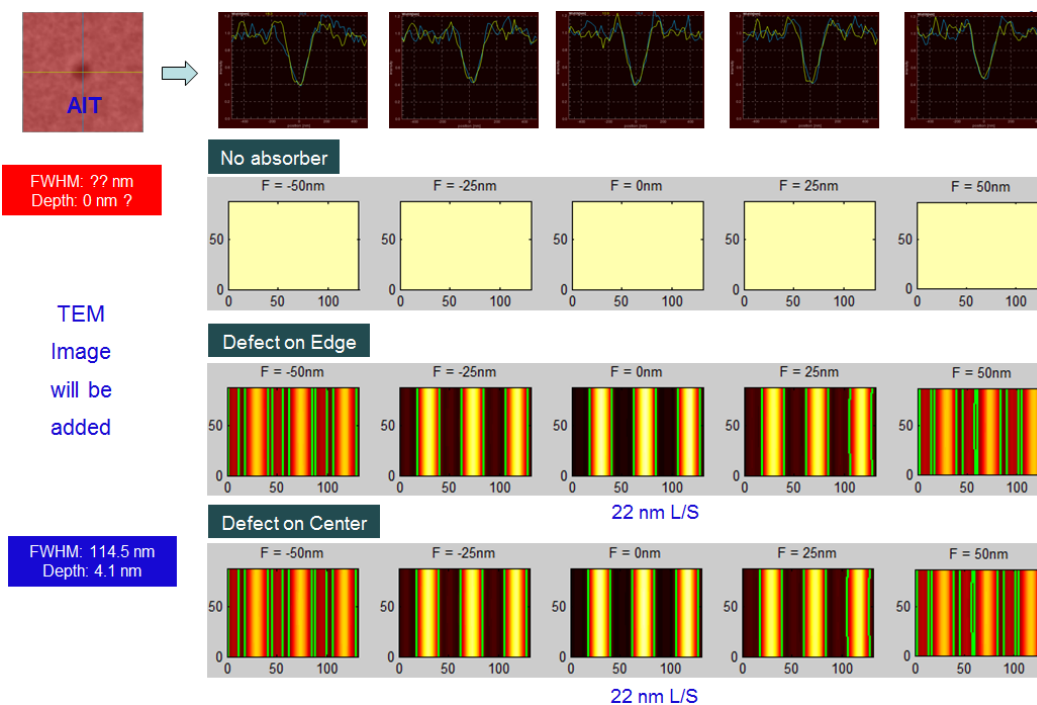


Figure 15. DPS images for a programmed ML phase defect. ML was deposited under pit smoothing conditions. Dimensions: FWHM of 114.5 nm with 4.1 nm depth at the bottom of the ML. No AFM image at the top of the ML.

### 3.6 DPS at different illumination conditions

Defect printability of a programmed ML phase defect at different illumination conditions was investigated as shown in figure 16. The ML was deposited under SEMATECH's BKM condition. The phase defect of 105 nm FWHM and 4.3 nm deep at the bottom of the ML printed under both illumination conditions when 22 nm L/S patterns were applied. Likewise, all programmed ML phase defects were simulated using DPS at 22 nm, 27 nm, and 32 nm L/S patterns using both illumination conditions and all phase defects were located at the edge of L/S patterns and at the center of space patterns for the simulation as well.

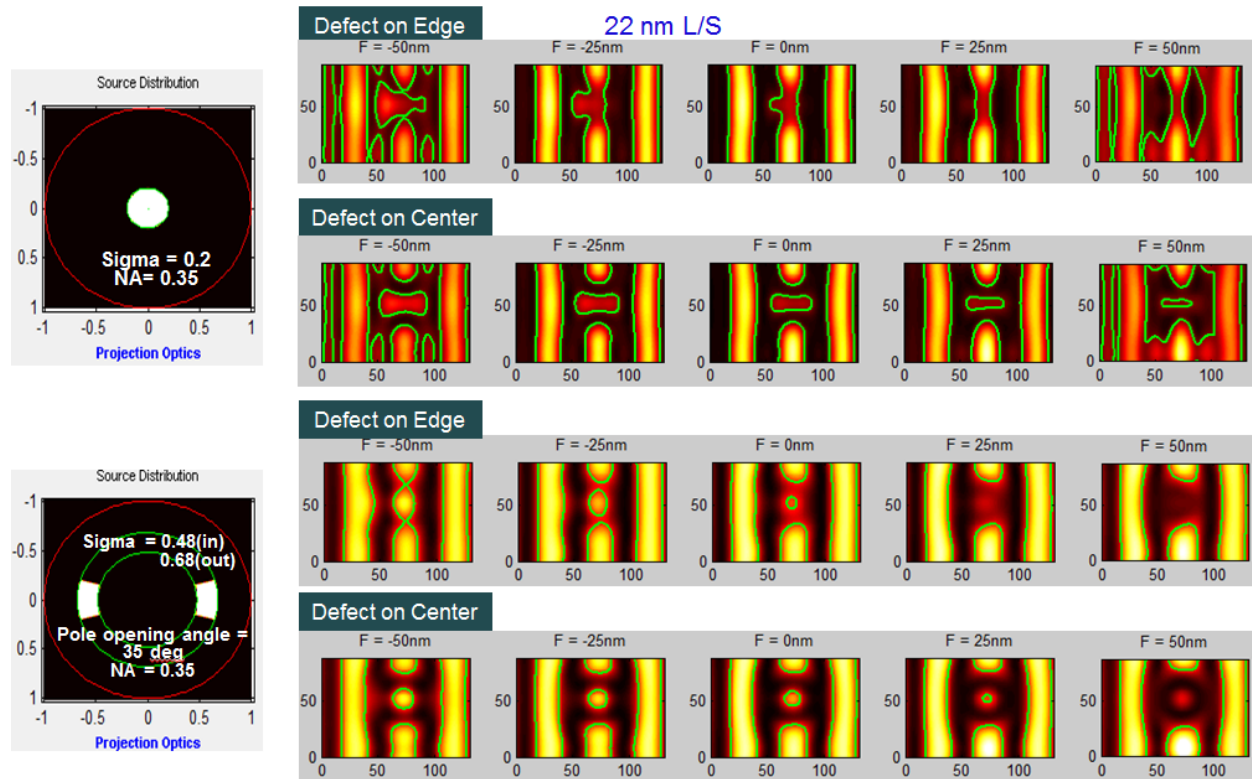


Figure 16. DPS images for a programmed ML phase defect under different illumination conditions. ML was deposited under SEMATECH's BKM condition. Dimensions: FWHM of 90.75 nm with 6.7 nm depth at the bottom of the ML and FWHM of 105.25 nm with 4.3 nm depth at the top of the ML.

### 3.7 Defect printability of L/S patterns

The printability of a programmed ML phase defects at L/S patterns is summarized in figures 17 and 18. The ML was deposited under SEMATECH's BKM condition. Defect printability results of figure 17 and figure 18 were obtained with a disc illumination of 0.2 sigma and 0.35 NA, and with a dipole illumination of 0.48(in)/0.68(out) sigma with a dipole opening angle of 35 degrees and 0.35 NA, respectively. Disc illumination results in wider printability process window than dipole illumination in 32 nm L/S patterns. On the other hand, dipole illumination shows a wider printability process window than dipole illumination in 27 nm L/S patterns. Defects at the edge of the L/S patterns have a wider printability process window than defects at the center of space patterns. However, defects in 22 nm L/S patterns have a very narrow process window only under disc illumination when the defects are located at the edge of L/S patterns. ML phase defects in 22 nm L/S pattern will be more critical issues and need to be addressed to develop more repair and defect avoidance techniques.

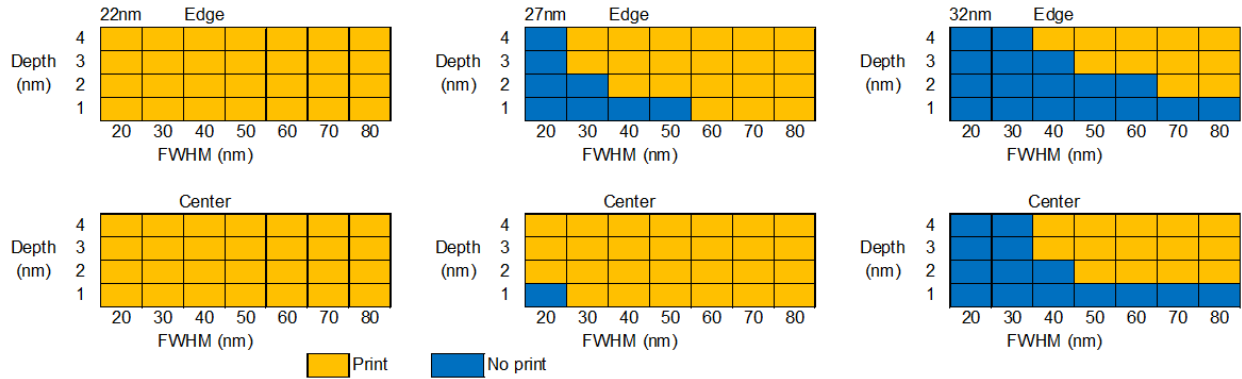


Figure 17. Defect printability of L/S patterns at the illumination condition of 0.2 sigma and 0.35 NA. ML was deposited under SEMATECH's BKM condition. Dimensions of FWHM and depth are at the bottom of ML. CDs for unprintable defects are 20 nm ~ 24 nm at 22 nm L/S patterns, 24.5nm ~ 29.5 nm at 27 nm L/S patterns, and 29 nm ~ 35 nm at 32 nm L/S patterns. Otherwise, all defects do print.

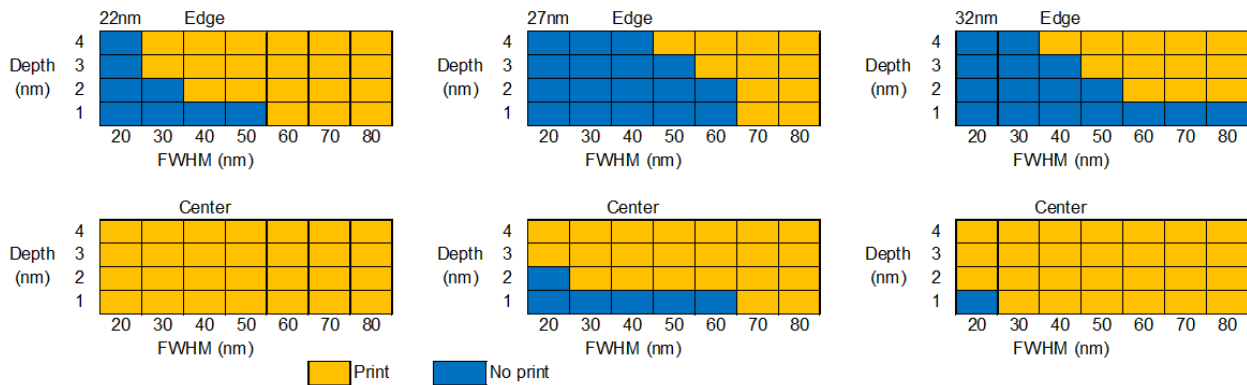


Figure 18. Defect printability of L/S patterns under the illumination condition of 0.48(in)/0.68(out) sigma with dipole opening angle of 35 degrees and 0.35 NA. ML was deposited under SEMATECH's BKM condition. Dimensions of FWHM and depth are at the bottom of the ML. CDs for unprintable defects are 20 nm ~ 24 nm at 22 nm L/S patterns, 24.5nm ~ 29.5 nm at 27 nm L/S patterns, and 29 nm ~ 35 nm at 32 nm L/S patterns. Otherwise, all defects do print.

#### 4. SUMMARY

ML phase defects are one of the major issues in adopting EUV lithography into production. Programmed defects were prepared on quartz substrates and MLs were deposited on top of programmed defects using SEMATECH's BKM and pit smoothing conditions to investigate defect decoration during ML deposition process. AFM and TEM images were used for ML defect printability simulations and MDR was successfully generated from AFM images of the ML top surface. MDR images match well with TEM images, and DPS intensity images show good correlation to AIT intensity images. DPS was used for 22 nm, 27 nm, and 32 nm L/S pattern printability on top of multilayer defects. Native multilayer defects need to be reduced for successful 22 nm and 27 nm wafer exposure. With our optical conditions, programmed defects at 27 nm L/S patterns are less printable using dipole illumination while defects at 32 nm L/S patterns are less printable using disc illumination.

## 5. FUTURE WORK

More programmed ML defect images from TEM need to be obtained. DPS under various illumination conditions will be done and L/S CDs with and without defects will be analyzed under various illumination conditions. The simulation results will be compared with the results from NXE3100 exposure of wafers.

## ACKNOWLEDGEMENTS

The author wants to express his thanks to R. Teki, J. Underwood, T. Owen, M. Maloney from SEMATECH for providing their efforts and tool time for this paper. The author also wants to thank to T. Nakajima, M. Kishimoto, and T. Uno from AGC; I. Mochi and K. A. Goldberg from LBNL; Y. Yamaguchi and H. Kinoshita from the Univ. of Hyogo; and V. Tolani, D. Peng, and L. Pang from Luminescent Technologies for their effort and resources in supporting experiments for this paper.

## REFERENCES

- [1] K. A. Goldberg, A. Barty, Y. Liu, P. Kearny, Y. Tezuka, T. Terasawa, J. S. Taylor, H. S. Han, and, O. R. Wood, "Actinic inspection of extreme ultraviolet programmed multilayer defects and cross-comparison measurements," *J. Vac. Sci. Technol. B* 24(6), 2824 (2006).
- [2] T. Yamane, T. Iwasaki, T. Tanaka, T. Terasawa, O. Suga, T. Tomie, "Actinic EUVL mask blank inspection and phase defect characterization," *Proc. SPIE* 7379, 73790H (2009)
- [3] H. J. Kwon, J. Harris-Jones, R. Teki, A. Cordes, T. Nakajima, I. Mochi, K. A. Goldberg, Y. Yamaguchi, H. Kinoshita, "Printability of native blank defects and programmed defects and their stack structures", *Proc. SPIE* 8166, 81660H (2011)
- [4] H. J. Kwon, J. Harris-Jones, T. Ranganath, V. Jindal, D. Chan, F. Goodwin, "Native Blank Defect Analysis for the Study of Printability," *EIPBN 2011, Las Vegas, (2011)*
- [5] R. Jonckheere, D. Heuvel, T. Bret, T. Hofmann, J. Magana, I. Aharonson, D. Meshulach, E. Hendrickx, and K. Ronse, "Evidence of printing blank-related defects on EUV masks missed by blank inspection," *Proc. SPIE* 7985, 79850W (2011)
- [6] T. Kamo, T. Terasawa, T. Yamane, H. Shigemura, N. Takagi, T. Amano, T. Tanaka, K. Tawarayama, O. Suga, and Ichiro Mori, "Printability of EUVL mask defect detected by actinic blank inspection tool and 199-nm pattern inspection tool," *Proc. SPIE* 7823, 78231U (2010)
- [7] H. J. Kwon, R. Teki, J. Harris-Jones, and A. Cordes, , "EUVL defect printability: an industry challenge," *Proc. SPIE* 8352, EMLC 8352-26 (2012)
- [8] H. J. Kwon, A. Cordes, R. Teki, and J. Harris-Jones, "Classification of multilayer defects and their printability," *EUVL Symposium 2011, Miami (2011)*